Solar Energy 190 (2019) 350–360

Contents lists available at ScienceDirect

Solar Energy

journal homepage: www.elsevier.com/locate/solener

Earth-abundant nontoxic direct band gap semiconductors for photovoltaic applications by *ab-initio* simulations

P.D. Sreedevi[a,b], R. Vidya[c], P. Ravindran[a,b,d,*]

[a] Department of Physics, Central University of Tamil Nadu, Thiruvarur, Tamil Nadu 610101, India
[b] Simulation Center for Atomic and Nanoscale MATerials (SCANMAT), Central University of Tamil Nadu, Thiruvarur, Tamil Nadu 610101, India
[c] Department of Medical Physics, Anna University, Chennai, Tamil Nadu 600025, India
[d] Center of Material Science and Nanotechnology and Department of Chemistry, University of Oslo, Box 1033, Blindern, N-0315 Oslo, Norway

ARTICLE INFO

Keywords:
Solar cells
Density functional theory
Electronic properties
Charge carrier effective mass

ABSTRACT

Direct band gap semiconductors with high optical absorption, high electrical conductivity, high carrier mobility, low reflectance and low recombination rate of charge carriers are needed for a variety of applications in solar energy conversion and optoelectronics. We have identified three ternary semiconductors Ca_3PN, NaBaP and ZrOS which have direct-band gap and other promising properties for solar energy applications. The prime novelty of this work mainly projects a detailed information on the electronic structure and optical properties for the three materials. From the first principles computational work and analysis, we have found that all the three materials with optimum band gap (~1.52 eV) value are having suitable absorption coefficient, extinction coefficient, optical conductivity and low reflectance in the visible region. Moreover, these materials are found to have low charge carrier effective masses and low recombination rates which can enhance carrier mobility and electrical conductivity. As a result, we will have three best non-silicon based direct band gap materials consisting of earth-abundant and non-toxic elements in the photovoltaic (PV) industry.

1. Introduction

Semiconductor materials having direct band gap values spanning visible and near infrared wavelengths have attracted broad interests in optoelectronic applications. This is mainly due to their spectacular achievements in the rate of absorption of photons that rivals the widely used indirect band gap silicon (Neamen, 1997; Hochbaum and Yang, 2010; Regulacio and Han, 2016). Monocrystalline silicon is widely used for photovoltaic applications which has an indirect band gap of 1.1 eV (Yuan et al., 2018; Putnam et al., 2010; Wilson, 1990). Nevertheless, the electronic transitions in the indirect band gap materials require the participation of phonons to ensure momentum conservation (Fatima et al., 2019; Zhang et al., 2001). Consequently, the efficiency of indirect band gap materials to absorb photons is relatively lower compared to the direct band gap materials. So, for solar cell applications, the direct band gap materials are more advantageous than the indirect band gap materials (Danan et al., 1987; Sun et al., 2017; Reddy et al., 2002; Xia et al., 2018). The maximum intensity of solar light is in the energy range from 1 eV to 4 eV (Nitz and Wilson, 1998) and the majority of the spectral irradiance is found at the energy of 1.52 eV. So, in order to maximize the number of photons absorbed, the energy band gap of the material should be equal or close to the band gap value of 1.52 eV (Bag et al., 2012; Shockley and Queisser, 1961). Therefore, we focus on identifying direct band gap semiconducting materials with band gap value close to 1.52 eV so that maximum solar energy can be harvested from the solar spectrum.

A number of non-silicon based materials CdTe (Cadmium Telluride) (Britt and Ferekides, 2012), GaAs (Gallium Arsenide) (Zhu and Liu, 2016), CIGS (Copper Indium Gallium Selenide) have a near optimum band gap (~1.52 eV) and large absorption coefficient. In addition, less abundance and toxicity of elements involved have environmental impacts. The above-mentioned widely adopted nonconventional materials have Cadmium, Arsenic, Tellurium, and Selenium which are highly toxic elements and hazardous to human health and environment (Alkorta et al., 2004). Moreover, Tellurium and Indium are very rare on earth (Bradshaw et al., 2013). Therefore, while exploring the possibilities of finding direct band gap semiconductors for photovoltaic applications, the material should satisfy availability on the one hand and non-toxicity of the constituent elements on the other (Cao et al., 2017).

From the systematic investigation of direct band gap semiconductors comprising of naturally abundant, less expensive and non-toxic elements (Jain et al., 2013), we have chosen three ternary

* Corresponding author.
E-mail address: raviphy@cutn.ac.in (P. Ravindran).

https://doi.org/10.1016/j.solener.2019.08.011
Received 8 May 2019; Received in revised form 13 July 2019; Accepted 5 August 2019
Available online 20 August 2019

semiconductors, Ca_3PN (Calcium Phosphide Nitride), NaBaP (Sodium Barium Phosphide) and ZrOS (Zirconium Oxysulphide) to check whether they have the promising properties for bringing them to the forefront of solar energy research.

Ca_3PN is a ternary nitride compound which belong in the family of antiperovskites (Bilal et al., 2015a, 2015b; Krivovichev, 2008; Peng et al., 2013). Over the last decade, because of the immense potential to solve energy issues, the antiperovskite compounds gained much attention (Bouhemadou and Khenata, 2007; Okoye, 2006; Ovsyannikov and Shchennikov, 2010; Sun et al., 2012). Among that, the group-2A based ternary antiperovskite compounds have been studied experimentally and theoretically by different researchers and different properties have been found (Amara et al., 2013; Belaroussi et al., 2008a, 2008b; Bidai et al., 2017, 2016; Bilal et al., 2015a, 2015b, 2015c 2014a, 2014b; Bouhemadou et al., 2007; Bouhemadou and Khenata, 2007; Chern et al., 1992a; Chi et al., 2002; Papaconstantopoulos, 1992; Dai and Ju, 2019; Gabler et al., 2004; Haddadi et al., 2010a, 2010b, Haddadi et al., 2009a, 2009b, Hichour et al., 2010, 2009; Hoat, 2019; Jha and Gupta, 2010; Iyigör and Selgin, 2019; Moakafi et al., 2009; Niewa et al., 2001; Okoye, 2006; Rahman et al.,2019; Shein and Ivanovskii, 2004; Sreedevi et al., 2019; Vansant et al., 1998). The synthesis of this antiperovskite compound was done by Chern et al. (1992b). They reported that this compound has a distorted orthorhombic structure due to small size of the P^{3-} ion and the electrical conductivity measurements showed insulating behaviour. The studies of pressure-dependent structural and electronic properties using Generalized Gradient Approximation, (GGA) were reported by Vansant et al. (1998). Using first-principles density functional theory (DFT) (Kohn et al., 1996; Hohenberg and Kohn, 1973) calculations, the effect of high pressures, up to 40 GPa, on the structural and elastic properties of Ca_3PN, was studied by Haddadi et al. (2009). Recently, the electronic and optical properties of cubic antiperovskites Ca_3MN (M = Ge, Sn, Pb, P, As, Sb and Bi) were investigated by Iqbal et al. (2016) by applying the full potential linearized augmented plane wave plus local orbitals (FP-LAPW + lo) scheme based on DFT.

Single crystals of NaBaP were obtained as a by-product in the synthesis of $Ba_6[Ga_2P_6]$ (Somer et al., 1996). ZrOS exists in cubic and tetragonal polymorphs (Jellinek et al., 1962; McCullough et al., 1948) and the cubic phase is found to have wide indirect band gap (Hautier et al., 2013). The cubic ZrOS is attractive as a transparent conducting material (Sarmadian et al., 2016; Sun et al., 2015). Even though structural properties were studied for tetragonal ZrOS in 1962, the other characteristics of this compound remain largely unexplored. So, we have paid special attention to the tetragonal phase of ZrOS.

The research group of Setyawan et al. (2011) has employed the high-throughput computational approach to screen up 193,456 compounds for potential new technological materials. In their article, they have reported the GGA band gap values and effective mass values for the compounds Ca_3PN and NaBaP. The similar type computational screening study was done by Kuhar (2018) in order to identify the materials with potential use as light absorbers in photovoltaics or photo electrochemical devices. They identified 74 materials. Among them, the considered three compounds are listed with their band gap values and effective mass values. In spite of these reported results on the three materials, there is still a lack of information about the optical properties for the compounds NaBaP and ZrOS, which is being addressed in the present article. Moreover, we have done an analysis of optical spectra with the help of orbital projected band structure. Such a study on the three materials has not been conducted earlier, to our knowledge. To get better insight in to their physical properties, we have performed the complete structural optimization, electronic structure, optical properties and charge carrier effective mass calculations. The present study is undertaken with the specific aim to bring out three non-silicon based materials with suitable physical properties applicable as solar cell absorbers. Since they contain earth abundant and non-toxic elements, the considered three materials will be advantageous for large-scale applications.

This article is organized as follows: The methodology and the computational techniques used in this work are presented in Section 2. Section 3 represents the results and discussions of the structural, electronic and optical properties. Finally the conclusions drawn are described in Section 4.

2. Methods

2.1. Compound selection screening approach

We used Density Functional Based Database (DFTBD) containing 1513 direct band gap values materials with band gap (E_g) values between 0.5 eV and 1.5 eV for the identification of suitable materials solar cell applications (Vajeeston). In our first screening, we disregarded the compounds containing toxic (e.g. Cd, Se, Pb, As etc), expensive (e.g. Te, In, Au, Ag, Pt, Cs etc), magnetic (Fe, Mn, Bi, Cu etc) and rare-earth elements. Then we have considered ternary compounds with naturally abundant elements. Since GGA was used for the band structure calculation in DFTBD, the compounds with band gap value in the range from 0.8 eV to 1 eV were reasonable for our selection because GGA underestimates the bandgap values up to 50%. Furthermore, we have considered the compounds having dispersed band extrema present in the Materials Project (Jain et al., 2013) database. The experimental crystal structure data of the considered three compounds were taken from the Inorganic Crystal Structure Database (ICSD) (Bergerhoff et al., 1983) for the present calculations.

2.2. Computational data

In this work, structural data taken from ICSD are optimized and their energies are computed using the DFT as implemented in Vienna Ab-initio simulation Package (VASP) (Hafner, 2009; Kresse and Hafner, 1993) within the Projector augmented Plane wave method (PAW) (Blöchl, 1994) together with the GGA functional proposed by Perdew-Burke-Ernzerh (PBE) (Perdew et al., 1996). For all the three compounds, a high plane wave energy cut-off of 800 eV with a Γ centered grid was used for optimizations of the crystal structures to obtain the structural parameters precisely (Patra et al., 2018). For the optimizations of the structures of Ca_3PN, NaBaP and ZrOS, we used the **k**-point (Pack and Monkhorst, 1977) set of $10 \times 10 \times 10$, $8 \times 8 \times 10$ and $10 \times 10 \times 8$, respectively. The optimizations are considered to be converged when the total energy of the system is stable within 1×10^{-6} eV/f.u. and the force acting on each atom is diminished until the maximum Hellmann-Feynman force (Parlinski et al., 1997) is less than 0.01 eV/Å. For Ca, 3*s*-3*p* and 4*s* electrons were treated as valence electrons. For P and N, 3*s*-3*p* and 2*s*-2*p* were included as the valence electrons, respectively. We have used the pseudopotentials separately for the atoms Na, Ba, Zr, O, S by using the 3*s*, 5*s*-5*p*-6*s*, 4*s*-4*p*-5*s*-4d, 2*s*-2*p* and 3*s*-3*p* configurations, respectively. The underestimated GGA band gap values were improved by using the hybrid DFT calculations. For the hybrid functional calculations, we have used the exchange-correlation energy functional HSE06 with a screening parameter of 0.2 Å (Henderson et al., 2011; Heyd et al., 2003; Muscat et al., 2001).

The advent of the electronic density of states (DOS) calculation led to the widespread knowledge on the chemical bonding behavior present in the compounds. So, the DOS was calculated using HSE06. From the PDOS, the orbital of each element giving rise to the different electronic states were identified. In addition, a Γ centered **k**-point mesh of $40 \times 40 \times 40$, $30 \times 30 \times 30$ and $32 \times 32 \times 32$ for Ca_3PN, NaBaP and ZrOS respectively, were used for the calculations of optical properties. In order to understand the origin of optical absorption peaks in more detail, we have done the analysis of orbital projected band structure analysis using Tight binding Linear Muffin-tin orbital (TB-LMTO) (Krier et al., 1994) method. For the LMTO computation, we have used the optimized structural parameters obtained from VASP calculations as input.

2.3. Effective mass calculation

The effective mass calculation of charge carriers were performed by VASPKIT (Wang, 2009), which is a post processing tool for the VASP code. The effective mass (m^*) of charge carriers was calculated by (Suzuki et al., 1995):

$$\frac{1}{m^*} = \frac{1}{\hbar}\frac{\partial^2 E(k)}{\partial k^2} \quad (1)$$

where m^* depends on the second derivative of the energy of the free electron Bloch wave with respect to the wave vector which is the decisive factor for curvature of the band dispersion at the extrema. Here, we have calculated the effective mass using finite difference method (FDM) (Cartoixà et al., 2003) as implemented in the VASPKIT. We have calculated the band structure with higher number of k-points in each direction in order to get more accurate value of effective mass for both electrons as well as holes.

3. Results and discussion

3.1. Structural properties

The total energies of Ca_3PN, NaBaP, and ZrOS have been calculated as a function of the unit cell volume. The equilibrium lattice parameters and bulk modulus follow from a fit of the total energy as a function of the volume to Murnaghan (1944) equation of state. The optimized crystal structures are represented in Fig. 1. Lattice parameters, atom positions, equilibrium volume (V_0) and bulk moduli (B_0) for Ca_3PN, NaBaP, and ZrOS, are given in Table 1, together with the available experimental results.

The equilibrium lattice constants obtained for Ca_3PN, NaBaP, and ZrOS are in good agreement with the available experimental values. Since we have done the structural optimization with the GGA, the lattice parameters and bond lengths are overestimated. The lattice constants a and c for NaBaP are overestimated by 0.94% and 0.59%, respectively. Similarly, for ZrOS, the lattice constants are overestimated by 1.77%, and 1.36%, respectively. As the deviations are small, we can consider that the agreement between experiment and theory is very good and DFT can accurately predict structural parameters for these compounds.

The compound Ca_3PN belongs to the antiperovskite type structure with space group of *Pm-3m*. It has a cubic structure with one formula unit per unit cell. From the Fig. 1(a), it is clear that the nitrogen atom is octahedrally coordinated with six calcium atoms. The crystal structure of NaBaP is hexagonal with a space group of *P-62m* and three formula units per unit cell. Here, for the better understanding of the crystal structure, we constructed a super cell of $2 \times 2 \times 1$ of NaBaP and shown the same in Fig. 1(b). From this supercell it is visible that each barium atom is in tetrahedral coordination with four phosphorous atoms. ZrOS crystallizes in a tetragonal type of structure with a space group of *P4nmm* and two formula units per unit cell.

3.2. Analysis of electronic structure

For a better understanding of the electronic, optical properties, and chemical bonding of these compounds, the analysis of band structures can be quite helpful. The electronic structure calculations are performed using the Generalized Gradient Approximation (GGA) which utilizes the gradient of the atomic charge density, thus overestimating the bonding interactions as implemented and eventually underestimates the band-gap. This is an inherent deficiency of DFT calculation with GGA. In order to overcome these issues, we used hybrid of Hartree-Fock (HF) and usual exchange-correlation functional as implemented in the HSE06 functional (Henderson et al., 2011; Heyd et al., 2003; Muscat et al., 2001). Fig. 2 corresponds to the calculated band structures of the above three compounds using PBE and HSE06 functionals and Fig. 3 depicts the calculated total density of states (TDOS) and partial density of states (PDOS) from HSE06 functional. From the band structure analysis, we found that the valence band maximum (VBM) and the conduction band minimum (CBM) occur at the Γ point for all three compounds which indicate their direct band gap behaviour.

The PBE calculated values of band gap (Γ-Γ) for Ca_3PN, NaBaP and ZrOS compounds are 0.81 eV, 0.85 eV and 0.81 eV, respectively; whilst, the HSE06 functional gives improved band gap values such as 1.63 eV, 1.52 eV and 1.64 eV, respectively for these compounds. Also, it is interesting to analyse the dispersion of electronic energy bands obtained from these two different functionals.

For all three compounds, it is highlighted that the increase of band gap is due to an upward shift of all the bands in the CB. Table 2 shows the individual shifts of the bottom of the CB ($\Delta E_{CB} = E_{CB}^{HSE06} - E_{CB}^{GGA}$) at the Γ point in the Brilliouin zone. However, the bands in the vicinity of VBM do not get perturbed by the change in exchange correlation functional in all the three compounds. In contrast, the bands in the lower energy region of the valence band systematically shifted to lower energy with respect to the bands obtained from PBE functional when we use the HSE06 functional. In all the three compounds we have noticed that the shift in the HSE06 derived bands is more when we move towards the lower energy region of the valence band. The orbital projected band structure obtained from TB-LMTO-ASA method showed a similar band dispersion characteristics as that obtained from VASP calculations. The orbital projected band structure obtained using GGA functional is helpful to analyze the characteristics of VB and CB. The disadvantage of direct band gap materials is that the probability of recombination is relatively high because of the direct transitions of electrons from CBM to VBM. The probability of carrier recombination will be lowered only when the photogenerated electrons and holes are spatially well separated from each other *i.e.* they sit in two different atoms. When this condition happens, then the probability of meeting the photo-excited electron and hole will be less. The low recombination rate is a desirable property for increasing the efficiency of solar cells.

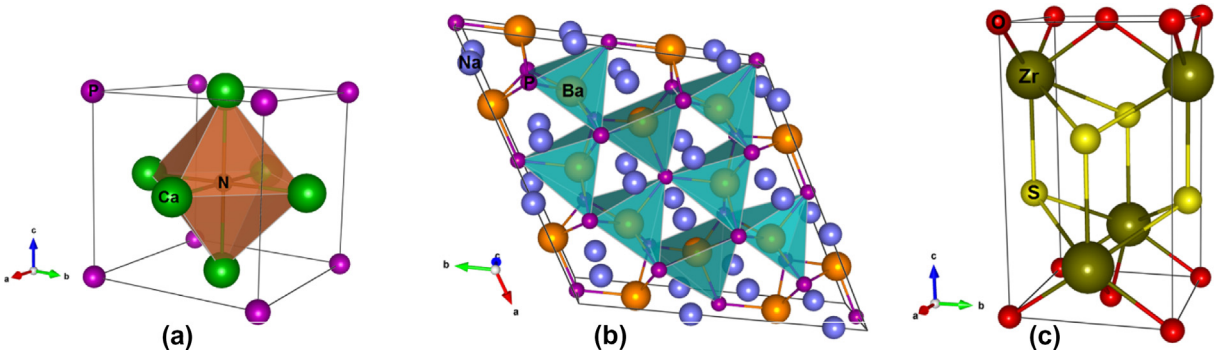

Fig. 1. Optimized crystal structures for (a) Ca_3PN, (b) NaBaP and (c) ZrOS.

Table 1
Theoretically calculated and experimentally observed (enclosed in bracket) structural parameters for Ca_3PN, NaBaP and ZrOS.

Compound (Space Group)	Unit Cell Parameters (Å)	Atom Positions	Optimized Volume per unit cell (Å^3)	Bulk Modulus B_0 (GPa)
Ca_3PN *(Pm-3m)*	a = 4.730 (4.730)[a]	Ca = 0, 0.5000, 0.5000 (0, 0.5000, 0.5000)[a] P = 0.5000, 0.5000, 0.5000 (0.5000, 0.5000, 0.5000)[a] N = 0, 0, 0 (0, 0, 0)[a]	105.82	63.23
NaBaP *(P-62m)*	a = 8.015 (7.940)[b] c = 4.703 (4.676)[b]	Na = 0.2420, 0, 0 (0.2380, 0, 0)[b] Ba = 0.5880, 0, 0.5000 (0.5853, 0, 0.5000)[b] P1 = 0.3333, 0.6667, 0 (0.3333, 0.6667, 0)[b] P2 = 0, 0, 0.5000 (0, 0, 0.5000)[b]	130.84	33.58
ZrOS *(P4nm)*	a = 3.613 (3.550)[c] c = 6.395 (6.310)[c]	Zr = 0, 0.5000, 0.1964 (0, 0.5000, 0.1950)[c] O = 0, 0, 0 (0, 0, 0)[c] S = 0, 0.5000, 0.6270 (0, 0.5000, 0.6330)[c]	83.50	160.85

[a] Chern et al. (1992b).
[b] Somer et al. (1996).
[c] McCullough et al. (1948).

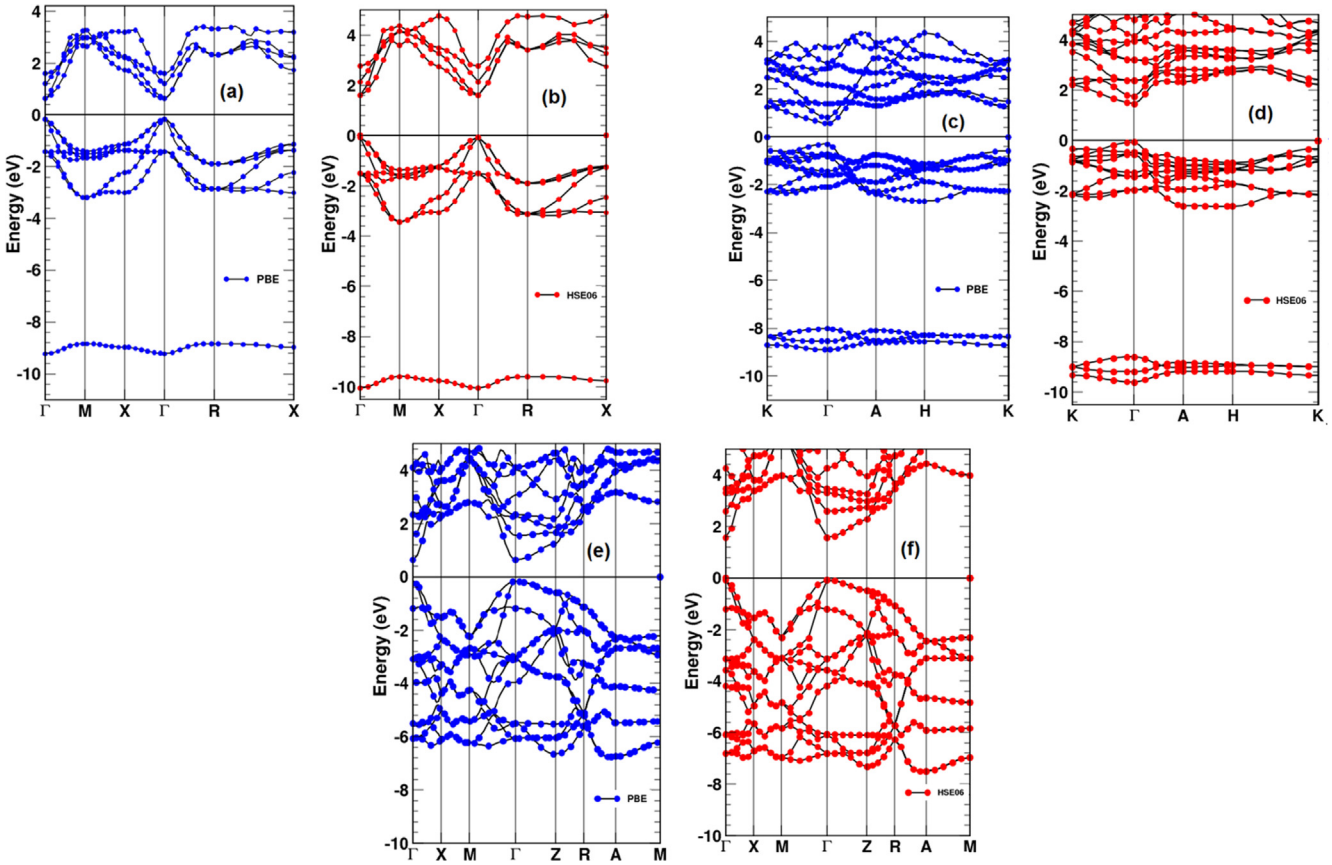

Fig. 2. The calculated band structures for (a) Ca_3PN-PBE, (b) Ca_3PN-HSE06, (c) NaBaP-PBE, (d) NaBaP-HSE06 (e) ZrOS-PBE, and (f) ZrOS-HSE06. The Fermi level is set to zero.

Here, from the analysis of orbital projected band structure and density of states, we have shown that the CBM and the VBM are originating from electronic states of two different atomic sites such that the photo-generated electrons and holes will be spatially located in two different atomic sites. As a consequence of this, the carriers in all these compounds will have relatively low recombination rate.

Table 2 shows the band gap values for the materials considered in comparison to previous calculated and experimental results. The experimental result (Chern et al., 1992b) of the semiconducting behaviour of Ca_3PN compound is well confirmed from our band structure results obtained from both PBE and HSE06 calculations. It is obvious from the Table that all our calculated values with GGA are well consistent with the previous GGA results. But our HSE06 band gap values are slightly different from what we can see from the previous results with other improved-band gap methods.

Our calculated GGA band gap values for Ca_3PN and NaBaP are 0.81 eV and 0.85 eV respectively, consistent with the other theoretical values 0.81 eV and 0.83 eV reported by Setyawan et al. (2011) for the respective compounds calculated by GGA. But in the study of Kuhar (2018), they have reported the band gap values as 2.46 eV, 2.22 eV and 1.7 eV for Ca_3PN, NaBaP and ZrOS, respectively, with GLLB-SC [Gritsenko, van Leeuwen, van Lenthe, and Baerends, (GLLB) with the correlation for solids (-SC)] correction method. These values are fairly different from our HSE band gap values (1.63 eV, 1.52 eV and 1.64 eV). One of the possible differences in the change in band gap values is the difference in the exchange correlation function we used. It is obvious

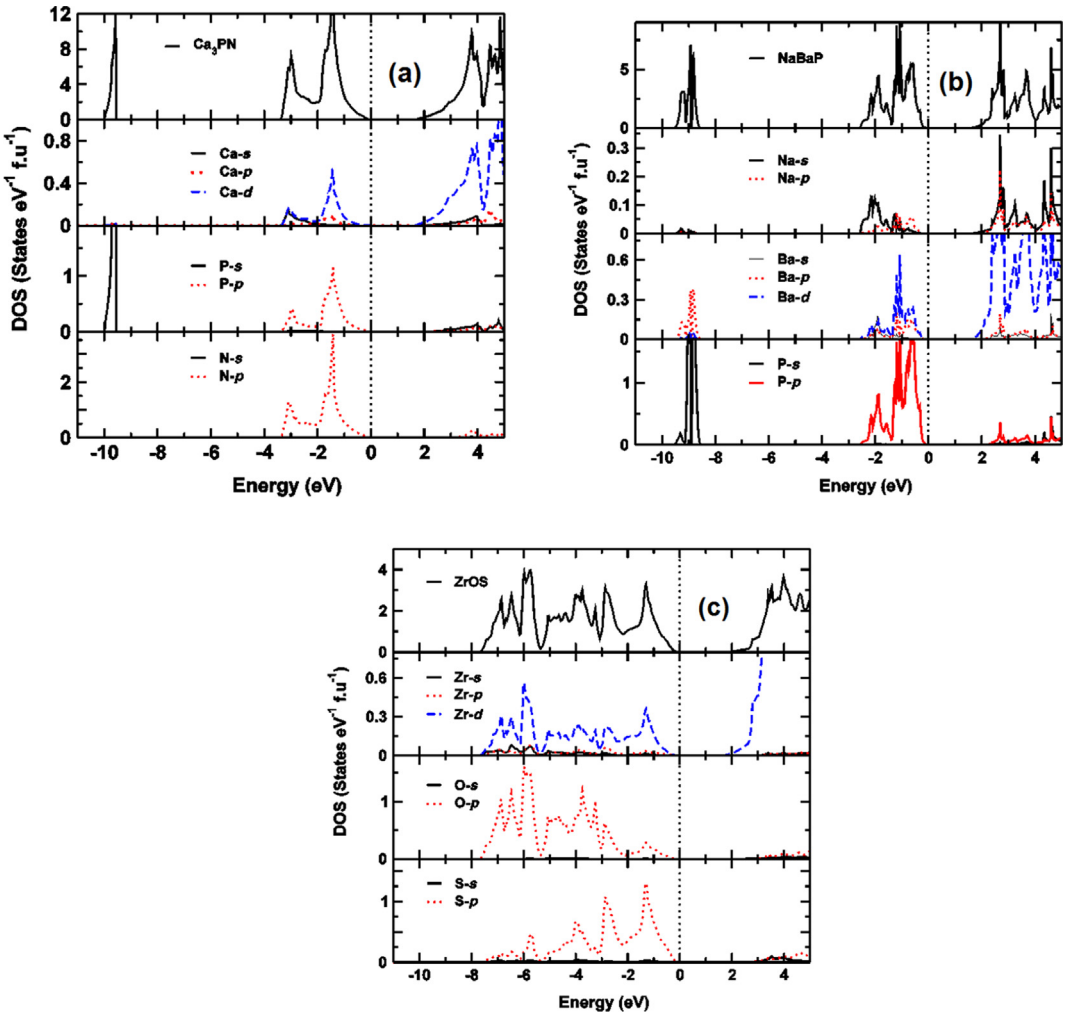

Fig. 3. Total and partial density of states for (a) Ca_3PN, (b) NaBaP and (c) ZrOS from HSE06 functional. The Fermi level is set to Zero.

Table 2
The position of conduction band edge of Ca_3PN, NaBaP and ZrOS from PBE (E_{CB}^{PBE}) and HSE06 (E_{CB}^{HSE06}) calculations and the shift in the conduction band edge (ΔE_{CB}) by the application of hybrid functional.

Compound	E_{CB}^{PBE} (eV)	E_{CB}^{HSE06} (eV)	ΔE_{CB} ($E_{CB}^{HSE06} - E_{CB}^{PBE}$) (eV)	Other reported band gap values (eV)
Ca_3PN	0.81	1.63	0.94	Insulator[a] 0.81[b] 1.49[c] 2.46[d]
NaBaP	0.85	1.52	0.92	0.83[b] 2.22[d]
ZrOS	0.81	1.64	0.99	1.7[d]

[a] Chern et al. (1992b).
[b] Setyawan et al. (2011).
[c] Iqbal et al. (2016).
[d] Kuhar (2018).

that different methodology yielded different band gaps values for the materials. Moreover, the input parameters taken for structural optimization may also contribute to the difference. In order to bench-mark our calculations, we have calculated band gaps for Si, GaAs and ZnO using HSE06 method and found that the experimental band-gaps are well reproduced. Hence the same methodology is adapted to predict the band-gap of these three compounds.

In the study by Castelli et al. (2014), it is clearly mentioned that the band gap values obtained by GLLB-SC correction method within an error of 0.5 eV are comparable to the other improved band gap methods like hybrid functional (HSE06) and GW. Also, in the paper by Iqbal et al. (2016), they have done the electronic structure with the very accurate method TB-MBJ (Tran-Blaha Modified Becke-Johnson) and EV-GGA (Engel-Vosko GGA) for the electronic band structure calculation. Using TB-MBJ method with fairly very high K-points (1000Kpoints) they are getting a band gap value of 1.49 eV for Ca_3PN and by EV-GGA (10,000 Kpoints), they obtained the band gap value of 1.72 eV for the same compound. These two values are fairly favourable to our improved band gap value for the cubic compound Ca_3PN.

Since HSE06 method is giving accurate electronic structure, we have compared and discussed the band structure calculated by HSE06 with the DOS for the three materials in the following sub-sections.

3.2.1. Ca_3PN

In Ca_3PN, one low lying valence band is located between −10 and −8 eV, which mainly arises from the electrons in the 3*s* orbital of phosphorous. The uppermost valence band is mainly contributed by the electrons from phosphorous $3p_y$ and $3p_z$ orbitals with noticeable contribution from the electrons at the 2*p* and $3p_x$ orbitals of nitrogen and phosphorous, respectively. The contribution of Ca *s* and *p* states to the VB is negligible. The bottommost conduction band stems from the $3d_{z2}$ orbitals of calcium. From the band structure it can be seen that the bands are more localized in the upper most valence band region and the localized bands can also be recognized from the DOS of this compound.

The DOS of this compound (Fig. 3(a)) shows that below the VBM,

the bands are equally dominated by 2*p* and 3*p* states of nitrogen and phosphorous. So, these two states are energetically degenerate indicating a strong covalent bonding between N and P. The contribution of 4*s* and 3*p* orbitals of Ca to the VB is negligibly small. This suggests that the Ca atom donates most of its valence electrons to the surrounding phosphorous and nitrogen atoms, forming an ionic bonding with Ca and PN cluster. But, the conduction band mainly comprises of the Ca-3*d* states and these *d* states are more concentrated above 2 eV energy region. From the PDOS obtained using HSE06, it is clear that the main bonding interaction in Ca_3PN is, ionic bonding between Ca and [PN] clusters with strong covalent bonding between N and P.

3.2.2. NaBaP

Our orbital – projected band structure results for the NaBaP show that the lowest three valence bands located between −10 and −8 eV are mainly originated by electrons from the 3*s* orbitals of phosphorous and the top of the valence band at the Γ point is mainly of $3p_z$ character originating from phosphorous and the other bands in the valence band consist of phosphorous $3p_x$ and $3p_y$ states. The three lowest energy bands in the VB are significantly affected by the HSE06 correction and shifted to lower energy as evident from Fig. 2b. Further, we notice that the bottommost conduction band arises mainly from the Ba- $3d_z^2$ states with significant contribution from the 3*s* states of Na. The bands in the higher energy range of CB mainly consist of the other 3*d* states of Ba.

The PDOS in Fig. 3(b) clearly shows that the P-3*p* states are more pronounced close to the top of the valence band. But, the contribution from Na is negligibly small in the valence band. The CB, mainly comprises of the Ba-5*d* and Na-3*s* states. From the PDOS, it is clear that the main bonding interaction between Ba and P in NaBaP is the hybridization between the P-3*p* and Ba-5*d* states and hence there is a finite covalent bonding present in this system. The density of states analysis show that the Na donates its valence electrons to the [BaP] cluster forming ionic bonding between Na and [BaP] whereas Ba and P form covalent interactions.

3.2.3. ZrOS

For ZrOS, the valence bands at the lower energy region consist of $2p_x$ and $2p_y$ states of oxygen. But the top of the valence band mainly arises from the $3p_x$ and $3p_y$ states of sulphur. The bottom of the conduction band originates from the electrons at the $4d_{x\text{-}y}^{2\,2}$orbitals of zirconium and the other bands in this conduction band mainly evolve from the electrons in the rest of the 4*d* orbitals of zirconium.

From the PDOS (Fig. 3(c)), it is seen that the valence band region is dominated by the S-3*p* and O-2*p* states. The CBM is mainly comprised of Zr-4*d*. From the PDOS, it is clear that the main bonding interaction between constituents in ZrOS is because of the hybridization among the O-2*p*, S-3*p* and Zr-4*d* states and hence the bonding interaction between the constitutes is mainly covalent in nature.

3.3. Optical properties

Studies of the optical properties of solids have been proven to be a powerful tool for understanding the electronic and atomic structure of semiconducting materials (Ahuja et al., 1999; Dadsetani and Pourghazi, 2006; Yang et al., 2010). We now turn to the analysis of the optical spectra for obtaining further insight into the electronic structure of these three compounds.

The imaginary part of the optical dielectric function, ε_2 (ω), is of fundamental importance and can be used to explain features of linear response of the system to electromagnetic radiation.

$$\varepsilon_2(\omega) = \frac{4\Pi e^2}{m^2\omega^2}\sum_{ij}\int \langle i|M|j\rangle^2 f_i(1-f_i)\delta(E_f - E_i - \omega)d^3\mathrm{k} \tag{2}$$

where M is the dipole matrix, I and j are the initial and final states respectively. The Fermi distribution function for the i^{th} state is represented as f_i and E_i is the electron energy in the i^{th} state. The real part of optical dielectric function, ε_1 (ω), can be derived from the corresponding imaginary part of dielectric function, ε_2 (ω), by the Kramer-Kronig relationship (Aspnes and Studna, 1983, Blaha et al., 2016).

All the frequency dependent linear optical properties such as refractive index *n*(ω), extinction coefficient *k*(ω), absorption coefficient *α*(ω), optical conductivity σ(ω), and reflectivity *R*(ω) can be obtained directly from the calculated ε_1 (ω) and ε_2(ω) (Ahuja et al., 1999; Dadsetani and Pourghazi, 2006; Karazhanov et al., 2007a; 2007b; Okoye, 2003; Ravindran et al., 2007, 1999, 1997; Saha et al., 2000; Yang et al., 2010).

$$\mathrm{n}(\omega) = \frac{((\varepsilon_1^2 + \varepsilon_2^2)^{1/2} + \varepsilon_1)^{1/2}}{\sqrt{2}} \tag{3}$$

$$\mathrm{k}(\omega) = \frac{((\varepsilon_1^2 + \varepsilon_2^2)^{1/2} - \varepsilon_1)^{1/2}}{\sqrt{2}} \tag{4}$$

$$\mathrm{L}(\omega) = \frac{\varepsilon_2(\omega)}{\varepsilon_1(\omega)^2 + \varepsilon_2(\omega)^2} \tag{5}$$

$$\mathrm{R}(\omega) = \left|\frac{\sqrt{\varepsilon(\omega)} - 1}{\sqrt{\varepsilon(\omega)} + 1}\right|^2 \tag{6}$$

$$\alpha(\omega) = \sqrt{2}(\omega)([\varepsilon_1^2 + \varepsilon_2^2]^{1/2} - \varepsilon_1(\omega))^{1/2} \tag{7}$$

$$\sigma(\omega) = \frac{\omega}{4\Pi}\varepsilon_2(\omega) \tag{8}$$

Here, we have plotted the optical spectra up to an energy range of 8 eV. For these three compounds, all the calculated optical spectra have been rigidly shifted based on the bandgap value obtained from HSE06 functional in order to correct for the DFT underestimation of the band gap values. For Ca_3PN, from experimental electrical conductivity measurements it is reported (Chern et al., 1992b) that this material is an insulator. However, no experimentally measured band gap value is given (Chern et al., 1992b). For NaBaP and ZrOS, no experimental data of electronic band structures are available. So, for these three compounds, the artificial shift technique has been applied to account for the underestimation of bandgap by PBE in all calculated optical spectra by taking the corresponding accurate band gap value obtained from the hybrid functional calculation. This rigid shift is 0.83 eV, 0.67 eV and 0.82 eV for Ca_3PN, NaBaP and ZrOS respectively.

Since the crystal structure of Ca_3PN is cubic, its optical properties are isotropic *i.e.* same along the crystallographic *a, b* and *c* axes. So, for the analysis, only one of the dielectric tensor components, $\varepsilon_{xx}(=\varepsilon_{yy}=\varepsilon_{zz})$ is sufficient for finding the other optical properties. The imaginary part of the optical dielectric function ε_2 (ω) is directly related to the polarizability of the crystal and provides information about the optical absorption of the materials. The condition where ε_2 (ω) is zero, then the material is said to be transparent until the absorption begins at which ε_2 (ω) will become non-zero.

The calculated imaginary part of the dielectric function of Ca_3PN is shown in Fig. 4(a). The main feature of ε_2 (ω) for Ca_3PN is that the peak with higher intensity present around 6 eV. We know that the optical spectra are originating from the inter-band transition of electrons from VB to CB. The interband optical transition analysis show that the peak around 6 eV corresponds mainly to the interband optical transitions arising from the VB originating from P-$3p_y$, N-$2p_x$ located in the VBM to Ca-$3d_{yz}$ states in the CB at 6 eV. The main feature in ε_1(ω) (see in Fig. 4(b)), is the sharp peak at 6 eV and the steep slope between 5.5 and 6.2 eV, after which ε_1(ω) becomes negative. The frequency at which the zero crossing of ε_1(ω) occurs corresponds to the location of plasma frequency (Sun et al., 2005). Plasma frequency is the frequency above which the materials show dielectric behaviour ($\varepsilon_1(\omega) > 0$), while below which they show metallic property ($\varepsilon_1(\omega) < 0$) (Brewer et al., 2005; Brewer and Franzen, 2004). The extinction coefficient, *k* (ω) (the

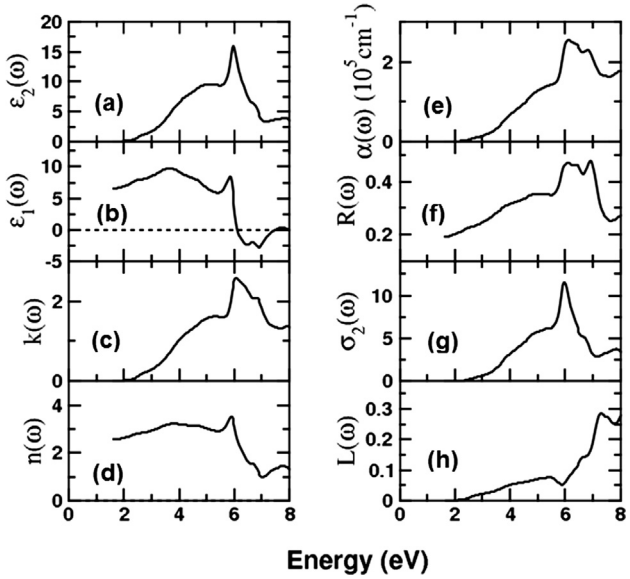

Fig. 4. The calculated optical spectra for Ca_3PN (a) and (b) dielectric parameters, (c) extinction coefficient k(ω), (d) refractive index n(ω), (e) absorption coefficient α(ω), (f) reflectivity R(ω), (g) Imaginary part of optical Conductivity $\sigma_2(\omega)$ and (h) EELS L(ω).

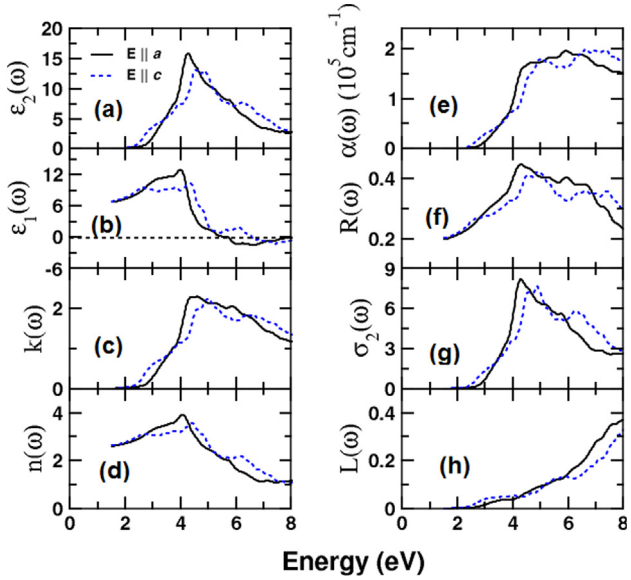

Fig. 5. The calculated optical spectra for NaBaP (a) and (b) dielectric parameters, (c) extinction coefficient k(ω), (d) refractive index n(ω), (e) absorption coefficient α(ω), (f) reflectivity R(ω), g) Imaginary part of optical Conductivity $\sigma_2(\omega)$ and (h) EELS L(ω).

imaginary part of the complex refractive index) (see Fig. 4(c)) show a sharp peak around 6 eV. The transition from P($3p_y$), N($2p_x$) to Ca($3d_{yz}$) may drive to the peak at this energy range.

The spectra of refractive indices $n(\omega)$ (Fig. 4(d)) of these compounds have similar frequency dependent features like $\varepsilon_1(\omega)$ spectra. The absorption spectra, $\alpha(\omega)$ (Fig. 4(e)) has a sharp peak at 6 eV and this may come from the inter-band optical transitions from P($3p_y$) and N($2p_x$) *to* Ca($3d_{yz}$) states. The absorption spectra is reasonably high and in the order of 10^5 cm^{-1}. The reflectivity shows less than 25% around the energy value of 2 eV. The imaginary part of optical conductivity spectrum for Ca_3PN is shown in Fig. 4(g) and the line shape of $\sigma_2(\omega)$ spectrum is having same spectral distribution as the ε_2 (ω) spectra due to the absorptive nature of the $\sigma_2(\omega)$ spectra.

The studies of Electron Energy Loss Spectrum (EELS) (Prytz et al., 2006; Simsek et al., 2014), L(ω), is the representation of characteristic energy loss (plasmon oscillations) which is important for the description of microscopic and macroscopic properties of solids. This function is proportional to the probability that a fast electron moving across a medium loses an energy E per unit length. In general, the highest peak in the L(ω) spectrum is considered as the plasmon peak and that is at 7 eV in L(ω) spectra (Fig. 4(h)) corresponds to that energy ε_1 (ω) = 0 (see in Fig. 4(b)), and this gives the plasma resonance.

Because of the hexagonal and tetragonal symmetries of NaBaP and ZrOS compounds, respectively, the resulting diagonal component of the dielectric spectra is a tensor and has two independent components $\varepsilon_{xx}(=\varepsilon_{yy})$ and ε_{zz}.

The frequency dependent imaginary ($\varepsilon_2(\omega)$) and real part (ε_1 (ω)) of dielectric function for NaBaP are depicted in Fig. 5(a) and (b), respectively. The imaginary part of the dielectric spectrum shows a maximum peak at 4.2 eV, but the amplitude of the peak is slightly decreased and varied when light polarised along the *c*-axis. This peak is due to the inter-band transition between P-$3p_x$ states to Ba- $5d_{xz}$ states. The characteristics of $\varepsilon_1(\omega)$ spectra of NaBaP is that, a peak is present at 4 eV when the light is polarized along *a*-axis and 4.1 eV along *c*-axis and after that $\varepsilon_1(\omega)$ becomes negative between 5.4 and 8 eV along *a*-axis and 6.7–8 eV when the light is polarised along *c*-axis, which indicates the presence of plasma resonance. At higher energies, the spectra gradually increase towards zero when light is polarized along *a* as well as *c* axes. From Fig. 5(b) it is clear that the amplitude of this spectra is higher when E||*a* than E||*c*. A relatively large optical anisotropy is present in this system and this is evident from the noticeable difference between these spectra along E||*a* and E||*c*. The frequency dependent extinction coefficient, *k* (ω), shown in Fig. 5(c) has a broad maximum at 4 eV along E|| *a*, whereas this peak is slightly decreased and varied to 4.3 eV when E||*c*. Also, it has a small peak at 6 eV for E||*a* and the amplitude of this peak is decreased when the light is polarized along c-axis. The interband optical transitions of electrons from P-*s* orbitals to Na-p_z is the origin for this peak.

Within the same photon energy, where a broad peak is seen in the *k* (ω) spectra, one could also see a peak in the $\alpha(\omega)$ spectra as depicted in Fig. 5(e). The variation of reflectance for NaBaP as a function of energy is displayed in Fig. 5(f). Around 2 eV, the reflectivity is lower than 25%. The spectra of imaginary part of optical conductivity, $\sigma_2(\omega)$ for NaBaP are shown in Fig. 5(g). The absorptive part in the conductivity spectrum increases and reaches a maximum value at 6 eV when E||*a* and at 6.2 eV when E||*c* for NaBaP. The spectra of the absorptive part of the optical conductivity of this compound also have similar frequency dependent features like $\varepsilon_2(\omega)$ spectra. In the EELS spectra depicted in Fig. 5(h) represents maximum peaks at 7 eV, and which is the plasma frequency above which the materials showing dielectric property and below which it has metallic nature.

Fig. 6(a)–(h) shows the calculated optical spectra for ZrOS. Here, the $\varepsilon_2(\omega)$ spectra show highest peaks at 6.5 and 6 eV along E||*a* and E||*c* axes, respectively. These peaks are due to the inter-band optical transitions of electrons from $2p_x$ and $2p_y$ orbitals of oxygen to the unoccupied electronic states originating from Zr-$4d_z^2$ orbital. It is to be noted that the peaks in optical spectra do not correspond to a single inter-band transition; since, many occupied and unoccupied bands may involve in the optical transitions within an energy corresponding to a particular peak. The frequency dependence, $\varepsilon_1(\omega)$, is also plotted in Fig. 6 (b) for ZrOS. For this compound also, $\varepsilon_1(\omega)$ spectra and $n(\omega)$ spectra show same features in the photon energy range considered in the present study. In ZrOS $\varepsilon_1(\omega)$ spectra shows a maximum peak at 5 eV along E||*a*, but this peak is present slightly different energy position in the $\varepsilon_1(\omega)$ spectra corresponding to E||*c*. In addition, the amplitude of this spectrum having higher value along E||*c*-axis than that along *a*-axis. The calculated absorption coefficient with respect to the photon energy for the ZrOS compound is depicted in Fig. 6(e).

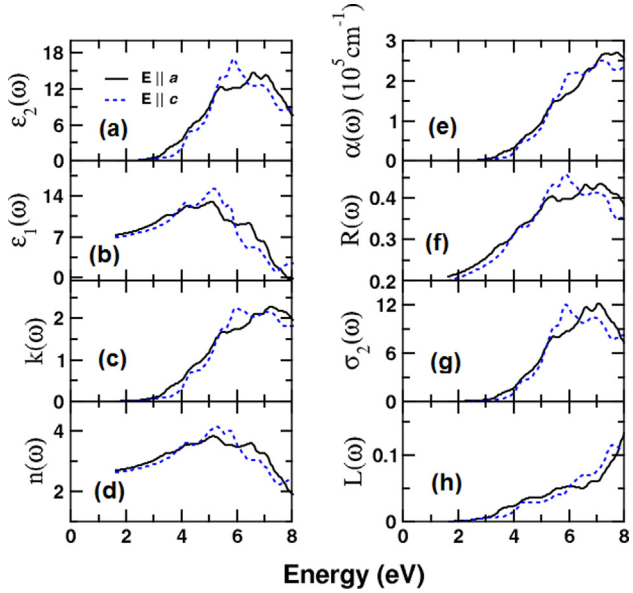

Fig. 6. The calculated optical spectra for ZrOS (a) and (b) dielectric parameters, (c) extinction coefficient k(ω), (d) refractive index n(ω), (e) absorption coefficient α(ω), (f) reflectivity R(ω), (g) Imaginary part of optical Conductivity $\sigma_2(\omega)$ and (h) EELS L(ω).

Also, for ZrOS, the absorption spectra $\alpha(\omega)$ (Fig. 6(e)) clearly show an exact resemblance with their corresponding $k(\omega)$ spectra (Fig. 6(c)) with peak positions also. The origin of peak at 5 eV in the $\alpha(\omega)$ are due to the optical inter-band transition of electrons from O ($2p_x$) and ($2p_y$) orbitals to Zr ($4d_z^2$) states. The variation of reflectance for ZrOS as a function of energy is displayed in Fig. 6(f). In the low-energy range, around 2 eV, the reflectance curves are having smaller than 25% reflectivity only. The imaginary part of optical conductivity spectra, $\sigma_2(\omega)$, for ZrOS is shown in Fig. 6(g). The peak in the optical conductivity spectra occurs at 6.5 and 6 eV for E||a and E||c, respectively for ZrOS. The spectra of the absorptive part of conductivity (σ_2 (ω)) of this compound also show similar frequency dependent features like the corresponding $\varepsilon_2(\omega)$ spectra. The peak in the L(ω) spectra (Fig. 6(h)) is present at 7 eV for E||a, but it is shifted to the lower energy to a value of 6.5 eV for E||c and corresponding energy values we could see zero value in the ε_1 (ω) spectra. It may be noted that the plasma resonance will occur in the energy values where we found peak in the L(ω) spectra.

The similarities in the optical properties of the three compounds considered for the present study are listed below.

1. The refractive indices of these compounds have similar frequency dependent features like $\varepsilon_1(\omega)$ spectra but peaks occur at different energies for different compounds.
2. The absorption spectra clearly show an exact resemblance with their corresponding $k(\omega)$ spectra with peak positions also.
3. The spectra of the absorptive part of conductivity of these compounds have similar frequency dependent features like the corresponding $\varepsilon_2(\omega)$ spectra.
4. The extinction coefficient and optical conductivity show peak with relatively high value in the visible energy region.
5. The absorption spectrum show large (about 10^5 cm^{-1}) value in the visible energy region for all the three compounds.
6. The reflectivity show a lower than 25% in the lower energy range around 2 eV and which indicates that these three compounds are transparent for photons with energy less than 2 eV.

So, along the optimum bandgap value with direct bandgap nature, the higher absorption coefficients, higher extinction coefficients, higher optical conductivity, and small reflectance in the visible energy region ensure the application of these semiconductors as ideal materials for high efficiency solar cells.

3.4. Effective mass of charge carriers

The effective mass of charge carriers is one of the important parameters of a semiconductor which determine the carrier transport properties (Liu et al., 2012). The transport of charge carrier in semiconductors is directly related to the electronic band structure (Larson et al., 2000; Vidal et al., 2012; Wang et al., 2015). Most importantly, the hole and electron effective masses are inversely proportional to the curvature of the relevant bands in the electronic band structure. In this section, we concentrate on the results of our calculations of hole and electron effective masses at the valence-band maxima and the conduction band minima for the three semiconductors considered in the present study. The procedure adopted to calculate effective mass (m^*) from band structure calculation is discussed in the computational section. In order to make test calculations for estimating effective masses for carrier we have used VASPKIT for some of the well-known semiconductors for which the experimental as well as theoretically calculated effective mass values are available in the literature (Araujo et al., 2013; Kim et al., 2010). The reliability of this method is quite good and well-grounded.

The results of the hole and electron effective masses along different crystallographic directions for the Ca_3PN, NaBaP and ZrOS are summarized and tabulated in Table 3. Other reported effective mass values for the concerned compounds are also added in Table 3. To the best of our knowledge, there are no experimental effective mass values reported for these three compounds. From Table 3, we can compare our results with the previous reported values. We cannot say that our results completely disagree with the available previous results. For the compound Ca_3PN, our values are showing good agreement with the effective mass values reported by Setyawan et al. (2011) and Kuhar, 2018). But for the phosphide compound NaBaP, the effective mass values along Γ→A are in good agreement with the results from Kuhar (2018) but fairly different with the results from Setyawan et al. (2011). As mentioned above that different methodology yielded different band gap values for the materials and that will also cause for the change in the carrier charge effective masses. In the effective mass calculation using VASPKIT, we have calculated the effective mass of charge carriers along different crystallographic directions that obviously will be different from values obtained from parabolic fitting method. For Ca_3PN, we have found and reported the charge carrier effective masses along Γ→X and Γ→R directions calculated using VASPKIT. Here we are generating the k-points vs energy along these two directions, then using finite

Table 3
Calculated carrier effective masses at the band edges for Ca_3PN, NaBaP and ZrOS in different crystallographic directions (in units of the free electron mass.).

	m^*_h (m_e)	m^*_e (m_e)
Ca_3PN		
Γ→X	0.460	0.419
Γ→R	0.399	0.291
Other reported values	0.38[a]	0.42[a]
	0.21[b]	0.29[b]
NaBaP		
Γ→A	0.135	0.227
Γ→K	2.776	0.405
Other reported values	0.76[a]	0.34[a]
	0.21[b]	0.25[b]
ZrOS		
Γ→X	0.489	0.352
Γ→Z	1.197	0.898
Other reported values	0.336[b]	0.347[b]

[a] Setyawan et al. (2011).
[b] Kuhar (2018).

difference method (FDM), we can attain the effective mass of charge carriers along these two directions. But in the parabolic fitting method, we have to consider the valence and conduction bands in the complete parabola, *i.e.* X→Γ→R. By taking the second derivative of the corresponding parabola, we can get the charge carrier effective mass values. And similarly, for the sulphide compound ZrOS, the charge carrier effective mass values are showing similar agreement with the effective mass values reported by Kuhar (2018).

For any material, low effective mass of the charge carriers implies high mobility of the carriers and consequently high conductivity. It is also reported that for any material to have excellent mobility of charge carriers, the effective masses should be less than $0.5m_o$ at least in one of the crystallographic directions (Ashwin Kishore and Ravindran, 2017; Bahers et al., 2014).

As we know, that effective masses of the charge carriers will be lower in the most dispersed bands since the effective mass is inversely proportional to the curvature of the corresponding bands in the band structure. This concept is well satisfied with the carrier effective mass values (in Table 3) at the band edges for Ca_3PN, NaBaP and ZrOS in different crystallographic directions. From the analysis of band extrema of Ca_3PN, it is clear that the bands along the Γ→X looks flatter than that along the Γ→R direction both at the VB and CB edges. Hence, the effective masses of charge carriers along the Γ→X direction are higher than that along the Γ→R direction. Interestingly, along these two crystallographic directions, the effective masses of the charge carriers are less than $0.5m_o$ which reflects their high mobility. Considering the effective mass values of NaBaP, we can see that along Γ→A, the electron effective mass is higher than the hole effective mass. From the band structure of NaBaP, it is evident that the valence band along Γ→A looks more dispersed that its corresponding conduction band, so that the change in effective masses occurred. And as a whole, one can observe from Fig. 2(d) that the curvature of the bands in the CBM and VBM along the Γ→A direction are more dispersed than those along Γ→K direction. In the case of ZrOS (Fig. 2(f)), the bands in the CBM and VBM along Γ→X direction is more dispersed than those along the Γ→Z direction. It is to be noted from Table 3 that for both NaBaP and ZrOS, the effective masses are lower along the Γ→A and the Γ→X directions, respectively. So, the carrier mobility of the charge carriers is expected to be higher along these dispersed directions. For these two compounds, the electron and hole effective masses are less than $0.5m_o$ along the directions where well dispersed bands are present. This implies that the mobility of the charge carriers will be high along these directions.

We have already discussed the recombination rate between electron and hole pairs in the 'Analysis of Electronic Structure' given in Section 3.2. With the carrier effective mass values also, we can get the information on the recombination rate pf electron-hole pairs. The relation between the recombination rate and the charge carrier effective mass as follows.

$$D = \frac{m_e^*}{m_h^*} \tag{9}$$

The high D value indicates that the electron and hole pairs are far apart from each other. Then the probability of meeting or recombine between electrons and holes will be lower (Ashwin Kishore and Ravindran, 2017). For our materials we are able to get the D value in the range of 0.7–1.7 except for NaBaP along Γ→K direction. So this is also one of the properties that influence the carrier mobility. The materials in which rate of recombination is less can exhibit high mobile charge carriers.

From the determination and analysis of the charge carrier effective masses in all considered three compounds, it is undoubtedly visible that the mobility of carriers will be higher and thus will have higher electrical conductivity.

4. Conclusion

In conclusion, we have presented a detailed investigation on the electronic structure, chemical bonding behavior, optical properties and carrier effective masses of three ternary direct band gap semiconductors: Ca_3PN, NaBaP and ZrOS using the first principles method. From the structural optimization calculations, we have found that the equilibrium lattice constants and positional parameters of all three semiconductors are in good agreement with the corresponding available experimental data. The electronic structure for the materials are performed using the most accurate method hybrid functional (HSE06) in addition to the usual GGA calculations. It was observed that, the three compounds are direct band gap semiconductors with optimum band gap values (~1.52 eV). From the analysis of orbital-projected band structure and density of states, it can be seen that the inter-band transitions are taking place between two different constituents in these ternary compounds and hence the recombination rate of the carriers would be lower. The presence of covalent hybridization in all the considered three compounds bring well dispersed bands which is resulting in low carrier effective mass and high mobility. The calculation of optical properties provides the information that the considered materials are showing higher absorption coefficients, higher extinction coefficients, higher optical conductivity and low reflectance in the visible energy region. Different inter-band transitions correspond to the peak intensities in the optical spectra which are explained with the help of orbital projected band structure. Effective mass calculations show the electron and hole effective masses are less than $0.5m_o$ along the directions where well dispersed bands are present and hence high carrier mobility along these directions are expected. So, these three compounds conform to the standards expected of high efficiency solar cells. Since they contain earth-abundant and non-toxic elements, the three materials can also be advantageous for large scale applications. The experimental research on the three considered compounds can be done for its practical applications since the experimental studies on similar compounds are available. As a result, we will have three best non-silicon based materials consisting earth-abundant and non-toxic elements in the photovoltaic (PV) industry.

Acknowledgements

This research was supported by the Indo-Norwegian Cooperative Program (INCP) via Grant No. F.No. 5812/2014(IC) and Department of Science and Technology, India via Grant No. SR/NM/NS1123/2013. P. Ravindran thank CSIR for the financial support through EMR-II project-03(1398).

The authors would like to acknowledge P. Vajeeston, for providing the Density Functional Theory Database (DFTBD) for this research work and Ms Ansu Elsa Ninan for the help in doing this work.

P. D. Sreedevi is grateful to Department of Medical Physics, Anna University, Chennai for hospitality.

All the crystal structures shown in this article were produced with the aid of VESTA (Momma and Izumi, 2011).

References

Ahuja, R., Eriksson, O., James, P., Johansson, B., 1999. Magnetic, optical, and magneto-optical properties of MnX (X = As, Sb, or Bi) from full-potential calculations. Phys Rev. B 59, 15680–15693. https://doi.org/10.1103/PhysRevB.59.15680.

Alkorta, I., Hernandez-Allica, J., Becerril, J.M., Amezaga, I., Albizu, I., G.C., 2004. Recent findings on the phytoremediation of soils contaminated with environmentally toxic heavy metals and metalloids such as zinc, cadmium, lead, and arsenic. Rev. Environ. Sci. Biotechnol. 3, 71–90.

Amara, K., Zemouli, M., Elkeurti, M., Belfedal, A., Saadaoui, F., 2013. First-principles study of $XNMg_3$(X = P, As, Sb and Bi) antiperovskite compounds. J. Alloys Compd. 576, 398–403. https://doi.org/10.1016/j.jallcom.2013.06.003.

Araujo, R.B., De Almeida, J.S., Ferreira Da Silva, A., 2013. Electronic properties of III-nitride semiconductors: a first-principles investigation using the Tran-Blaha modified Becke-Johnson potential. J. Appl. Phys. 114. https://doi.org/10.1063/1.4829674.

Ashwin Kishore, M.R., Ravindran, P., 2017. Tailoring the electronic band gap and band

edge positions in the C_2N monolayer by P and As substitution for photocatalytic water splitting. J. Phys. Chem. C 121, 22216–22224. https://doi.org/10.1021/acs.jpcc.7b07776.
Aspnes, D.E., Studna, A.A., 1983. Dielectric functions and optical parameters of Si, Ge, GaP, GaAs, GaSb, InP, InAs, and InSb from 1.5 to 6.0 eV. Phys. Rev. B 27, 985–1009. https://doi.org/10.1103/PhysRevB.27.985.
Bag, S., Gunawan, O., Gokmen, T., Zhu, Y., Todorov, T.K., Mitzi, D.B., 2012. Environmental science low band gap liquid-processed CZTSe solar cell with 10.1% efficiency. Energy Environ. Sci. 1–6. https://doi.org/10.1039/c2ee00056c.
Bahers, T. Le, Rerat, M., Sautet, P., 2014. Semiconductors used in photovoltaic and photocatalytic devices: assessing fundamental properties from DFT. J. Phys. Chem. C 118, 5997–6008. https://doi.org/10.1021/jp409724c.
Belaroussi, T., Amrani, B., Benmessabih, T., Iles, N., Hamdache, F., 2008a. Structural and thermodynamic properties of antiperovskite $SbNMg_3$. Comput. Mater. Sci. 43, 938–942. https://doi.org/10.1016/j.commatsci.2008.02.006.
Belaroussi, T., Benmessabih, T., Hamdache, F., Amrani, B., 2008b. First-principles study of the structural and thermodynamic properties of $AsNMg_3$ antiperovskite. Physica B 403, 2649–2653. https://doi.org/10.1016/j.physb.2008.01.047.
Bergerhoff, G., Hundt, R., Sievers, R., Brown, I.D., 1983. The inorganic crystal structure data base. J. Chem. Inf. Model. 23, 66–69. https://doi.org/10.1021/ci00038a003.
Bidai, K., Ameri, M., Amel, S., Ameri, I., Al-Douri, Y., Varshney, D., Voon, C.H., 2017. First-principles calculations of pressure and temperature dependence of thermodynamic properties of anti-perovskite $BiNBa_3$ compound. Chin. J. Phys. 55, 2144–2155. https://doi.org/10.1016/j.cjph.2017.03.023.
Bidai, K., Ameri, M., Ameri, I., 2016. A first-principles study on structural, thermodynamics and elastic properties of $XNBa_3$(X = As, Sb) under pressure and temperature effect. Optik 127, 3150–3157. https://doi.org/10.1016/j.ijleo.2015.12.076.
Bilal, M., Ahmad, I., Asadabadi, S.J., Ahmad, R., Maqbool, M., 2015a. Thermoelectric properties of metallic antiperovskites AXD_3 (A = Ge, Sn, Pb, Al, Zn, Ga; X = N, C; D = Ca, Fe, Co). Electron. Mater. Lett. 11, 466–480. https://doi.org/10.1007/s13391-015-4425-2.
Bilal, M., Ahmad, I., Rahnamaye Aliabad, H.A., Jalali Asadabadi, S., 2014a. Detailed DFT studies of the band profiles and optical properties of antiperovskites $SbNCa_3$ and $BiNCa_3$. Comput. Mater. Sci. 85, 310–315. https://doi.org/10.1016/j.commatsci.2013.12.035.
Bilal, M., Ahmad, R., Ahmad, I., 2015b. Electronic properties of antiperovskite materials from state-of-the-art density functional theory. J. Chem. 2015, 1–11.
Bilal, M., Khan, B., Rahnamaye Aliabad, H.A., Maqbool, M., Jalai Asadabadi, S., Ahmad, I., 2014b. Thermoelectric properties of $SbNCa_3$ and $BiNCa_3$ for thermoelectric devices and alternative energy applications. Comput. Phys. Commun. 185, 1394–1398. https://doi.org/10.1016/j.cpc.2014.02.001.
Bilal, M., Saifullah, Shafiq, M., Khan, B., Rahnamaye Aliabad, H.A., Jalali Asadabadi, S., Ahmad, R., Ahmad, I., 2015c. Antiperovskite compounds $SbNSr_3$ and $BiNSr_3$: potential candidates for thermoelectric renewable energy generators. Phys. Lett. A 379, 206–210. https://doi.org/10.1016/j.physleta.2014.11.016.
Blaha, P., Schwarz, K., Madsen, G.K.H., Kvasnicka, D., Luitz, J., 2016. Wien2K Code, An Augmented Plane Wave Plus Local Orbitals Program for Calculating Crystal Properties. Vienna University of Technology, Vienna, Austria.
Blöchl, P.E., 1994. Projector augmented-wave method. Phys. Rev. B 50, 17953–17979. https://doi.org/10.1103/PhysRevB.50.17953.
Bouhemadou, A., Khenata, R., 2007. Ab initio study of the structural, elastic, electronic and optical properties of the antiperovskite $SbNMg_3$. Comput. Mater. Sci. 39, 803–807. https://doi.org/10.1016/j.commatsci.2006.10.003.
Bouhemadou, A., Khenata, R., Chegaar, M., Maabed, S., 2007. First-principles calculations of structural, elastic, electronic and optical properties of the antiperovskite $AsNMg_3$. Phys. Lett. A 371, 337–343. https://doi.org/10.1016/j.physleta.2007.06.030.
Bradshaw, A.M., Reuter, B., Hamacher, T., 2013. The potential scarcity of rare elements for the Energiewende. Green 3, 93–111. https://doi.org/10.1515/green-2013-0014.
Brewer, S.H., Franzen, S., 2004. Calculation of the electronic and optical properties of indium tin oxide by density functional theory. J. Chem. Phys. 300, 285–293. https://doi.org/10.1016/j.chemphys.2003.11.039.
Brewer, S.H., Wicaksana, D., Maria, J.P., Kingon, A.I., Franzen, S., 2005. Investigation of the electrical and optical properties of iridium oxide by reflectance FTIR spectroscopy and density functional theory calculations. J. Chem. Phys. 313, 25–31. https://doi.org/10.1016/j.chemphys.2004.11.014.
Britt, J., Ferekides, C., 2012. Thinfilm CdS/CdTe solar cell with 15. 8 % efficiency thin-film. Appl. Phys. Lett. 2851, 14–16. https://doi.org/10.1063/1.109629.
Cao, X., Kawamura, F., Ninomiya, Y., Taniguchi, T., Yamada, N., 2017. Conduction-band effective mass and bandgap of $ZnSnN_2$ earth-abundant solar absorber. Sci. Rep. 7, 14987. https://doi.org/10.1038/s41598-017-14850-7.
Cartoixà, X., Ting, D.Z.Y., McGill, T.C., 2003. Numerical spurious solutions in the effective mass approximation. J. Appl. Phys. 93, 3974–3981. https://doi.org/10.1063/1.1555833.
Castelli, I.E., Hüser, F., Pandey, M., Li, H., Thygesen, K.S., Seger, B., Jain, A., Persson, K.A., Ceder, G., Jacobsen, K.W., 2014. New light-harvesting materials using accurate and efficient bandgap calculations. Adv. Energy Mater. 5, 1–7. https://doi.org/10.1002/aenm.201400915.
Chern, M.Y., Disalvo, F.J., Parise, J.B., Goldstone, J.A., 1992a. The structural distortion of the anti-perovskite nitride Ca_3AsN. J. Solid State Chem. 96, 426–435. https://doi.org/10.1016/S0022-4596(05)80277-4.
Chern, M.Y., Vennos, D.A., Disalvo, F.J., 1992b. Synthesis, structure, and properties of anti-perovskite nitrides Ca_3MN, M = P, As, Sb, Bi, Ge, Sn, and Pb. J. Solid State Chem. 96, 415–425. https://doi.org/10.1016/S0022-4596(05)80276-2.
Chi, E.O., Kim, W.S., Hur, N.H., Jung, D., 2002. New Mg-based antiperovskites $PnNMg_3$ (Pn = As, Sb). Solid State Commun. 121, 309–312. https://doi.org/10.1016/S0038-1098(02)00011-X.
Papaconstantopoulos, D.A., W.E.P., 1992. Ternary nitrides $BiNCa_3$ and $PbNCa_3$: Unusual ionic bonding in the antiperovskite structure. Phys. Rev. B 45.
Dadsetani, M., Pourghazi, A., 2006. Optical properties of strontium monochalcogenides from first principles. Phys. Rev. B 73, 1–7. https://doi.org/10.1103/PhysRevB.73.195102.
Dai, Jun, Ju, Ming-Gang, 2019. Bi(Sb)NCa_3: expansion of perovskites photovoltaics into all-inorganic anti-perovskite materials. J. Phys. Chem. C.
Danan, G., Etienne, B., Mollot, F., Planel, R., Jean-Louis, A.M., Alexandre, F., Jusserand, B., Le Roux, G., Marzin, J.Y., Savary, H., Sermage, B., 1987. Optical evidence of the direct-to-indirect-gap transition in GaAs-AlAs short-period superlattices. Phys. Rev. B 35, 6207–6212.
Neamen, Donald A., 1997. Semiconductor Physics and Devices. McGraw-Hill, New York.
Sun, Du., Xiong, Yihuang, 2017. Solution-synthesized In_4SnSe_4 semiconductor micriwires with a direct band gap. Chem. Mater. 29 (3), 1095–1098.
Fatima, Yulun Han, 2019. Photoexcite electron lifetimes influenced by momentum dispersion in silicon nanowires. J. Phys. Chem. C 123, 7457–7466.
Krier, G., Jepsen, O., Burkhardt, A., Andersen, O.K., 1994. The TB-LMTO-ASA program.
Gabler, F., Kirchner, M., Schnelle, W., Schwarz, U., Schmitt, M., Rosner, H., Niewa, R., 2004. $(Sr_3N)E$ and $(Ba_3N)E$ (E = Sb, Bi): synthesis, crystal structures, and physical properties. Z. Anorg. Allg. Chem. 630, 2292–2298. https://doi.org/10.1002/zaac.200400256.
Haddadi, K., Bouhemadou, A., Louail, L., 2010a. Ab initio investigation of the structural, elastic and electronic properties of the anti-perovskite $TlNCa_3$. Solid State Commun. 150, 932–937. https://doi.org/10.1016/j.ssc.2010.02.024.
Haddadi, K., Bouhemadou, A., Louail, L., 2010b. Structural, elastic and electronic properties of the hexagonal anti-perovskites $SbNBa_3$ and $BiNBa_3$. Comput. Mater. Sci. 48, 711–718. https://doi.org/10.1016/j.commatsci.2010.03.015.
Haddadi, K., Bouhemadou, A., Louail, L., Maabed, S., Maouche, D., 2009a. Structural and elastic properties under pressure effect of the cubic antiperovskite compounds $ANCa_3$ (A = P, As, Sb, and Bi). Phys. Lett. A 373, 1777–1781. https://doi.org/10.1016/j.physleta.2009.03.016.
Haddadi, K., Bouhemadou, A., Louail, L., Medkour, Y., 2009b. Structural, elastic and electronic properties of $XNCa_3$ (X = Ge, Sn and Pb) compounds. Solid State Commun. 149, 619–624. https://doi.org/10.1016/j.ssc.2009.01.025.
Haddadi, K., Bouhemadou, A., Louail, L., Rahal, F., Maabed, S., 2009c. Prediction study of the structural, elastic and electronic properties of $ANSr_3$ (A = As, Sb and Bi). Comput. Mater. Sci. 46, 881–886. https://doi.org/10.1016/j.commatsci.2009.04.028.
Hautier, G., Miglio, A., Ceder, G., Rignanese, G.M., Gonze, X., 2013. Identification and design principles of low hole effective mass p-type transparent conducting oxides. Nat. Commun. 4, 1–7. https://doi.org/10.1038/ncomms3292.
Henderson, T.M., Paier, J., Scuseria, G.E., 2011. Accurate treatment of solids with the HSE screened hybrid. Phys. Status Solidi B 248, 767–774. https://doi.org/10.1002/pssb.201046303.
Heyd, J., Scuseria, G.E., Ernzerhof, M., 2003. Hybrid functionals based on a screened Coulomb potential. J. Chem. Phys. 118, 8207–8215. https://doi.org/10.1063/1.1564060.
Hichour, M., Khenata, R., Rached, D., Hachemaoui, M., Bouhemadou, A., Reshak, A.H., Semari, F., 2010. FP-APW + lo study of the elastic, electronic and optical properties for the cubic antiperovskite $ANSr_3$ (A = As, Sb and Bi) under pressure effect. Physica B 405, 1894–1900. https://doi.org/10.1016/j.physb.2010.01.069.
Hichour, M., Rached, D., Rabah, M., Benalia, S., Khenata, R., Semari, F., 2009. Structural and elastic properties of antiperovskites $XNBa_3$ (X = As, Sb) under pressure effect. Physica B 404, 4034–4038. https://doi.org/10.1016/j.physb.2009.07.154.
Hoat, D.M., 2019. Structural, optoelectronic and thermoelectric properties of anti-perovskite compounds Ae_3PbS (Ae = Ca, Sr and Ba). Phys. Lett. A.
Hochbaum, A.I., Yang, P., 2010. Semiconductor nanowires for energy conversion. Chem. Rev. 110, 527–546.
Iqbal, S., Murtaza, G., Khenata, R., Mahmood, A., Yar, A., Muzammil, M., Khan, M., 2016. Electronic and optical properties of Ca_3MN (M = Ge, Sn, Pb, P, As, Sb and Bi) antiperovskite compounds. J. Electron. Mater. 45, 4188–44196. https://doi.org/10.1007/s11664-016-4563-9.
Iyigör, Ahamet, Selgin, Al, 2019. A comprehensive study on physical propertes of anti-perovskite $GeNCa_3$. SAUJS 23 (4), 1.
Hafner, J., 2009. Ab-initio simulations of materials using VASP: density-functional theory and beyond. J. Comput. Chem. 28, 73–86. https://doi.org/10.1002/jcc.
Jain, A., Ong, S.P., Hautier, G., Chen, W., Richards, W.D., Dacek, S., Cholia, S., Gunter, D., Skinner, D., Ceder, G., Persson, K.A., 2013. Commentary: the materials project: a materials genome approach to accelerating materials innovation. APL Mater. 1. https://doi.org/10.1063/1.4812323.
Jellinek, F., Songstad, J., Viljanto, J., 1962. A tetragonal form of zirconium oxdie suflide ZrOS. Acta Chem. Scand. (1989).
Jha, P.K., Gupta, S.K., 2010. First principles lattice dynamical study of the cubic anti-perovskite compounds $AsNBa_3$ and $SbNBa_3$. Solid State Commun. 150, 1650–1655. https://doi.org/10.1016/j.ssc.2010.06.037.
Kuhar, K., 2018. High-throughput computational assessment of previously synthesized semiconductors for photovoltaic and photoelectrochemical devices. ACS Energy Lett. 3. https://doi.org/10.1021/acsenergylett.7b01312.
Karazhanov, S.Z., Ravindran, P., Kjekshus, A., Fjellvåg, H., Svensson, B.G., 2007a. Electronic structure and optical properties of ZnX (X = O, S, Se, Te): a density functional study. Phys. Rev. B 75, 155104. https://doi.org/10.1103/PhysRevB.75.155104.
Karazhanov, S.Z., Ravindran, P., Vajeeston, P., Ulyashin, A., Finstad, T.G., Fjellvåg, H., 2007b. Phase stability, electronic structure, and optical properties of indium oxide polytypes. Phys. Rev. B 76, 1–13. https://doi.org/10.1103/PhysRevB.76.075129.

Kim, Y.S., Marsman, M., Kresse, G., Tran, F., Blaha, P., 2010. Towards efficient band structure and effective mass calculations for III–V direct band-gap semiconductors. Phys. Rev. B 82, 1–11. https://doi.org/10.1103/PhysRevB.82.205212.

Kohn, W., Becke, A.D., Parr, R.G., 1996. Density functional theory of electronic structure. J. Phys. Chem. 100, 12974–12980. https://doi.org/10.1021/jp960669l.

Kresse, G., Hafner, J., 1993. Ab initio molecular dynamics for liquid metals. Phys. Rev. B 47, 558–561. https://doi.org/10.1103/PhysRevB.47.558.

Krivovichev, S.V., 2008. Minerals with antiperovskite structure: a review. Z. Kristallog. 223, 109–113. https://doi.org/10.1524/zkri.2008.0008.

Larson, P., Mahanti, S., Kanatzidis, M.G., 2000. Electronic structure and transport of Bi_2Te_3 and $BaBiTe_3$. Phys. Rev. B 61, 8162–8171. https://doi.org/10.1103/PhysRevB.61.8162.

Yuan, Lin Ding, Deng, Hui-Xiong, 2018. Unified theory of irect or indirect band-gap natur of conventional semiconductors. Phys. Rev. B 98, 245203.

Liu, H.R., Chen, S., Zhai, Y.T., Xiang, H.J., Gong, X.G., Wei, S.H., 2012. First-principles study on the effective masses of zinc-blend-derived Cu_2Zn-IV-VI_4 (IV = Sn, Ge, Si and VI = S, Se). J. Appl. Phys. 112. https://doi.org/10.1063/1.4759322.

McCullough, J.D., Brewer, L., Bromley, L.A., 1948. The crystal structure of zirconium oxysulfide, ZrOS. Acta Crystallogr. 1, 287–289. https://doi.org/10.1107/S0365110X4800079X.

Moakafi, M., Khenata, R., Bouhemadou, A., Semari, F., Reshak, A.H., Rabah, M., 2009. Elastic, electronic and optical properties of cubic antiperovskites $SbNCa_3$ and $BiNCa_3$. Comput. Mater. Sci. 46, 1051–1057. https://doi.org/10.1016/j.commatsci.2009.05.011.

Momma, K., Izumi, F., 2011. VESTA 3 for three-dimensional visualization of crystal, volumetric and morphology data. J. Appl. Crystallogr. 44, 1272–1276. https://doi.org/10.1107/S0021889811038970.

Murnaghan, F.D., 1944. Proc. Natl. Acad. Sci. U. S. A 30, 244–247.

Muscat, J., Wander, A., Harrison, N.M., 2001. On the prediction of band gaps from hybrid functional theory. Chem. Phys. Lett. 342, 397–401. https://doi.org/10.1016/S0009-2614(01)00616-9.

Niewa, R., Schnelle, W., Wagner, F.R., 2001. Synthesis, crystal structure, and physical properties of $(Ca_3N)Tl$. Z. Anorg. Allg. Chem. 627, 365–370. https://doi.org/10.1002/zaac.201500738.

Nitz, P., Wilson, H.R., 1998. Switchable glazing with a large dynamic range in total solar energy transmittance (TSET). Sol. Energy 62, 215–228. https://doi.org/10.1016/S0038-092X(98)00014-0.

Okoye, C.M.I., 2006. First-principles optical calculations of $AsNMg_3$ and $SbNMg_3$. Mater. Sci. Eng., B 130, 101–107. https://doi.org/10.1016/j.mseb.2006.02.066.

Okoye, C.M.I., 2003. Theoretical study of the electronic structure, chemical bonding and optical properties of KNbO3 in the paraelectric cubic phase. J. Phys. Condens. Matter 15, 5945.

Ovsyannikov, S.V., Shchennikov, V.V., 2010. High-pressure routes in the thermoelectricity or how one can improve a performance of thermoelectrics. Chem. Mater. 635–647. https://doi.org/10.1021/cm902000x.

Hohenberg, P., Kohn, W., 1973. Inhomogeneous electron gas. Phys. Rev. B 7, 1912–1919. https://doi.org/10.1103/PhysRevB.7.1912.

Vajeeston P. (private communication).

Pack, J.D., Monkhorst, H.J., 1977. "Special points for Brillouin-zone integrations" – a reply. Phys. Rev. B 16, 1748–1749. https://doi.org/10.1103/PhysRevB.16.1748.

Parlinski, K., Li, Z.Q., Kawazoe, Y., 1997. First-principles determination of the soft mode in cubic ZrO_2. Phys. Rev. Lett. 78, 4063–4066. https://doi.org/10.1103/PhysRevLett.78.4063.

Patra, L., Pan, Z., Chen, J., Azuma, M., Ravindran, P., 2018. Metamagnetism stabilized giant magnetoelectric coupling in ferroelectric: $xBaTiO_3$–$(1–x)BiCoO_3$. Phys. Chem. Chem. Phys. 20. https://doi.org/10.1039/c7cp07677k.

Peng, T., Bo-sen, W., Yu-ping, S., 2013. Mn-based antiperovskite functional materials: review of research. Chin. Phys. B 22, 1–13. https://doi.org/10.1088/1674-1056/22/6/067501.

Perdew, J.P., Burke, K., Ernzerhof, M., 1996. Generalized gradient approximation made simple. Phys. Rev. Lett. 77, 3865–3868. https://doi.org/10.1103/PhysRevLett.77.3865.

Prytz, Ø., Løvvik, O.M., Taftø, J., 2006. Comparison of theoretical and experimental dielectric functions: electron energy-loss spectroscopy and density-functional calculations on skutterudites. Phys. Rev. B 74, 1–8. https://doi.org/10.1103/PhysRevB.74.245109.

Putnam, M.C., Boettcher, S.W., Kelzenberg, M.D., Turner-Evans, D.B., Spurgeon, J.M., Warren, E.L., Briggs, R.M., Lewis, N.S., Atwater, H.A., 2010. Si microwire-array solar cells. Energy Environ. Sci. 1037. https://doi.org/10.1039/c0ee00014k.

Rahman, Md Taslimur, 2019. Elastic, electronic and thermoelectric properties of Sr_3MN (M = Sb, Bi) under pressure. J. Alloys Compd. 783, 593–600.

Ravindran, P., Delin, A., Ahuja, R., Johansson, B., 1997. Optical properties of monoclinic SnI_2 from relativistic first-principles theory. Phys. Rev. B 56, 6851–6861.

Ravindran, P., Delin, A., Johansson, B., Eriksson, O., 1999. Electronic structure, chemical bonding, and optical properties of ferroelectric and antiferroelectric NaNO2. Phys. Rev. B 59, 1776–1785.

Ravindran, P., Vidya, R., Kjekshus, A., Fjellvåg, H., Eriksson, O., 2007. Theoretical investigation of magnetoelectric behavior in $BiFeO_3$. Phys. Rev. B 74, 2244412. https://doi.org/10.1103/PhysRevB.74.224412.

Reddy, K.M., Manorama, S.V., Reddy, A.R., 2002. Bandgap studies on anatase titanium dioxide nanoparticles. Mater. Chem. Phys. 78, 239–245.

Regulacio, M.D., Han, M., 2016. Multinary I-III-VI2 and I2-II-IV-VI 4 semiconductor nanostructures for photocatalytic applications. Acc. Chem. Res. 49, 511–519. https://doi.org/10.1021/acs.accounts.5b00535.

Saha, S., Sinha, T.P., Mookerjee, A., 2000. Electronic structure, chemical bonding, and optical properties of paraelectric $BaTiO_3$. Phys. Rev. B 62, 8828–8834.

Sarmadian, N., Saniz, R., Partoens, B., Lamoen, D., 2016. Easily doped p-type, low hole effective mass, transparent oxides. Sci. Rep. 6, 1–9. https://doi.org/10.1038/srep20446.

Setyawan, W., Gaume, R.M., Lam, S., Feigelson, R.S., Curtarolo, S., 2011. High-throughput combinatorial database of electronic band structures for inorganic scintillator materials. ACS Combust. Sci. 13, 382–390.

Shein, I.R., Ivanovskii, A.L., 2004. Electronic band structure and chemical bonding in the new antiperovskites $AsNMg_3$ and $SbNMg_3$. J. Solid State Chem. 177, 61–64. https://doi.org/10.1016/S0022-4596(03)00309-8.

Shockley, W., Queisser, H.J., 1961. Detailed balance limit of efficiency of pn junction solar cells. J. Appl. Phys. 32, 510–519. https://doi.org/10.1063/1.1736034.

Simsek, S., Koc, H., Trepakov, V.A., Mamedov, A.M., Ozbay, E., Koc, H., Trepakov, V.A., Mamedov, A.M., Ozbay, E., 2014. Electron spectroscopy and the electronic structure of $KNbO_3$: first principle calculations electron spectroscopy and the electronic structure of $KNbO_3$: first principle calculations. Ferroelectrics 461, 99–105. https://doi.org/10.1080/00150193.2014.889998.

Somer, M., Peters, E., Peters, K., Festkörperforschung, M., 1996. Crystal structure of sodium barium phosphide, NaBaP. Z. Kristallog. 13, 1996.

Sreedevi, P.D., Ravindran, P., Vidya, R., 2019. First principles prediction of the ground state crystal structures of antiperovskite compounds A_3PN (A = Be, Mg, Ca, Sr, Ba and Zn). Mater. Today: Proc.

Sun, J., Shi, H., Du, M.H., Siegrist, T., Singh, D.J., 2015. Ba_2TeO as an optoelectronic material: first-principles study. J. Appl. Phys. 117, 109–113.

Sun, J., Wang, H.T., He, J., Tian, Y., 2005. Ab initio investigations of optical properties of the high-pressure phases of ZnO. Phys. Rev. B 71, 1–5. https://doi.org/10.1103/PhysRevB.71.125132.

Sun, Y., Wang, C., Huang, Q., Guo, Y., Chu, L., Arai, M., Yamaura, K., 2012. Neutron diffraction study of unusual phase separation in the antiperovskite nitride Mn_3ZnN. Inorg. Chem. 7232–7236. https://doi.org/10.1021/ic300978x.

Suzuki, M., Uenoyama, T., Yanase, A., 1995. First-principles calculations of effective-mass parameters of AlN and GaN. Phys. Rev. B 52, 8132–8139. https://doi.org/10.1103/PhysRevB.52.8132.

Vansant, P., Van Camp, P., Van Doren, V., Martins, J., 1998a. Variable-cell-shape-based structural optimization applied to calcium nitrides. Phys. Rev. B 57, 7615–7620. https://doi.org/10.1103/PhysRevB.57.7615.

Vansant, P.R., Camp, P.E. Van, Doren, V.E. Van, Martins, J.L., 1998b. $AsNCa_3$ at high pressure. Comput. Mater. Sci. 10, 298–301.

Vidal, J., Lany, S., D'Avezac, M., Zunger, A., Zakutayev, A., Francis, J., Tate, J., 2012. Band-structure, optical properties, and defect physics of the photovoltaic semiconductor SnS. Appl. Phys. Lett. 100, 1–4. https://doi.org/10.1063/1.3675880.

Wang, V., 2009. VASPKIT, a post-processing tool for ab-initio code VASP.

Wang, V., Liu, Y.C., Kawazoe, Y., Geng, W.T., 2015. Role of interlayer coupling on the evolution of band edges in few-layer phosphorene. J. Phys. Chem. Lett. 6, 4876–4883. https://doi.org/10.1021/acs.jpclett.5b02047.

Wilson, I.H., 1990. In: Handbook of Semiconductor Silicon Technology. NOYES Publications, Park Ridge, New Jersey. https://doi.org/10.1080/00207219108925500. 795 pp., $96 (hardback). ISBN 0 8155 1237 6. Int. J. Electron. 71, 557–557.

Yang, L.-M., Vajeeston, P., Ravindran, P., Fjellvåg, H., Tilset, M., 2010. Theoretical Investigations on the chemical bonding, electronic structure, and optical properties of the metal − organic framework MOF-5. Inorg. Chem. 49, 10283–10290. https://doi.org/10.1021/ic100694w.

Zhang, P., Crespi, V.H., Chang, E., Louie, S.G., Cohen, M.L., 2001. Computational design of direct-bandgap semiconductors that lattice-match silicon. Nature 409, 69–71.

Xia, Zhiguo, Fang, Huajing, 2018. $CsCuSe_5$: a copper-rich ternary chalcogenide with nerly direct band gap for photovoltaic application. Chem. Mater. 3, 1121–1126.

Zhu, H.X., Liu, J., 2016. Electronic structure of organometal halide perovskite $CH_3NH_3BiI_3$ and optical absorption extending to infrared region. Sci. Rep. 6, 1–9. https://doi.org/10.1038/srep37425.